EFFECT OF HETEROGENEOUS ROUGHNESS PATCH ARRANGEMENT IN TURBULENT CHANNEL FLOW

Simon Dalpke, Carola Schmidt, Andreas Nettekoven, Alexander Stroh, Bettina Frohnapfel
Institute of Fluid Mechanics
Karlsruhe Institute of Technology
Kaiserstr. 10, 76131 Karlsruhe, Germany
simon.dalpke@kit.edu

ABSTRACT

The effects of different heterogeneous rough surfaces are investigated by analyzing three canonical configurations combining smooth and rough areas, namely streamwise and spanwise roughness strips as well as a checkerboard pattern. All surfaces share the same smooth-to-rough area ratio but differ in their spatial arrangement. In previous experiments with similar surface patterns, clear differences in the global friction drag were reported. Using direct numerical simulations, we identify flow features of the particular surface patterns, e.g., meandering high-velocity regions in the checkerboard-type roughness and the repeated formation of internal boundary layers. For the checkerboard-case, spatial heterogeneities are observed in the dispersive velocity, and the repeated formation of stress bores is visible downstream of surface condition transitions.

INTRODUCTION

In technical applications, rough surfaces may exhibit heterogeneous characteristics due to preferential orientation during operation, e.g., the directional wear in aeroengines or grouped barnacle accumulation on a ship hull. While the flow resistance of homogeneous rough surfaces is rather well understood, it is still challenging to reliably predict the global drag of a heterogeneous rough surface. For heterogeneous roughness, it was found that the effective skin friction coefficient for the same roughness coverage can change depending on the particular roughness arrangement (Schmidt *et al.*, 2026; Jensen & Forooghi, 2025). In order to examine characteristic flow phenomena of different configurations of roughness heterogeneity, we investigate turbulent channel flows with canonical heterogeneous rough surfaces at 50% roughness coverage composed of strips and patches of roughness, as shown in fig. 1.

METHODOLOGY

We solve the incompressible Navier-Stokes equations for a Newtonian fluid with constant fluid properties in a canonical channel setup. The corresponding dimensionless governing equations read as follows using the coordinate system indicated in fig. 1:

$$\frac{\partial u_i}{\partial x_i} = 0 \tag{1}$$

$$\frac{\partial u_j}{\partial t} + u_i \frac{\partial u_j}{\partial x_i} = -\frac{\partial p}{\partial x_j} + \frac{1}{Re_\tau}\frac{\partial^2 u_j}{\partial x_i^2} + \Pi_j \tag{2}$$

where $Re_\tau = \frac{u_\tau \delta}{\nu}$. A forcing in streamwise direction $\Pi_j = [1,0,0]^\mathsf{T}$ drives the fluid flow and yields a constant friction Reynolds number Re_τ. The simulations are performed with the highly scalable, GPU-accelerated finite difference solver `CaNS` (Costa, 2018) on a staggered Cartesian grid, where periodic boundary conditions are set for the streamwise and spanwise direction. The roughness is introduced at the top and bottom walls by an immersed boundary method (IBM) that enforces the no-slip condition using a volume-penalization approach (Shi *et al.*, 2025). The roughness is positioned in such a way that the meltdown height k_{md} of the rough surface coincides with the wall location of the smooth surface sections. This location forms the zero point for the wall-normal coordinate ($y = 0$). Hence, the wall-normal extent of the simulation domain is $L_y = 2(\delta + k_{\mathrm{md}})$ where δ corresponds to the effective channel half-height. The immersed boundary method as well as the GPU-accelerated code was successfully validated against literature results.

Four different configurations are investigated, summarized in fig. 1. The channel streamwise and spanwise dimensions are $6\delta \times 3\delta$ and $8\delta \times 8\delta$ for smaller and larger strip widths and patches, respectively. The 1.5δ wide roughness strips and $1.5\delta \times 1.5\delta$ roughness patches, as well as the $4\delta \times 4\delta$ patches, are placed symmetrically on bottom and top wall of the channel. Simulations are performed for $Re_\tau = 180$ for the small-sized heterogeneity, whereas the larger patch size is simulated for three different friction Reynolds numbers, namely $Re_\tau \in \{360; 500; 1000\}$. This results in increasing patch size in viscous units such that the patch side length s is given by $s^+ \in \{1440; 2000; 4000\}$.

For the statistical analysis the velocity fields are temporally and spatially averaged. The time-averaging operator is represented by $\bar{\cdot}$, whereas the intrinsic spatial averaging is indicated by $\langle\cdot\rangle$ and computed using the void fraction ϕ of the fluid-filled domain

$$\langle\cdot\rangle = \frac{1}{\phi(x_2)}\frac{1}{A}\int\int \cdot \,\mathrm{d}x_1\,\mathrm{d}x_3, \tag{3}$$

where ϕ is computed as the ratio of fluid area $A_f(x_2)$ to total area A. The dimensionless bulk velocity is computed using an intrinsic average

$$U_b = \frac{1}{\delta}\int_{-k_{md}}^{\delta} \langle \bar{u}_1 \rangle \,\mathrm{d}x_2. \tag{4}$$

The numerical simulations are complemented by hot-wire

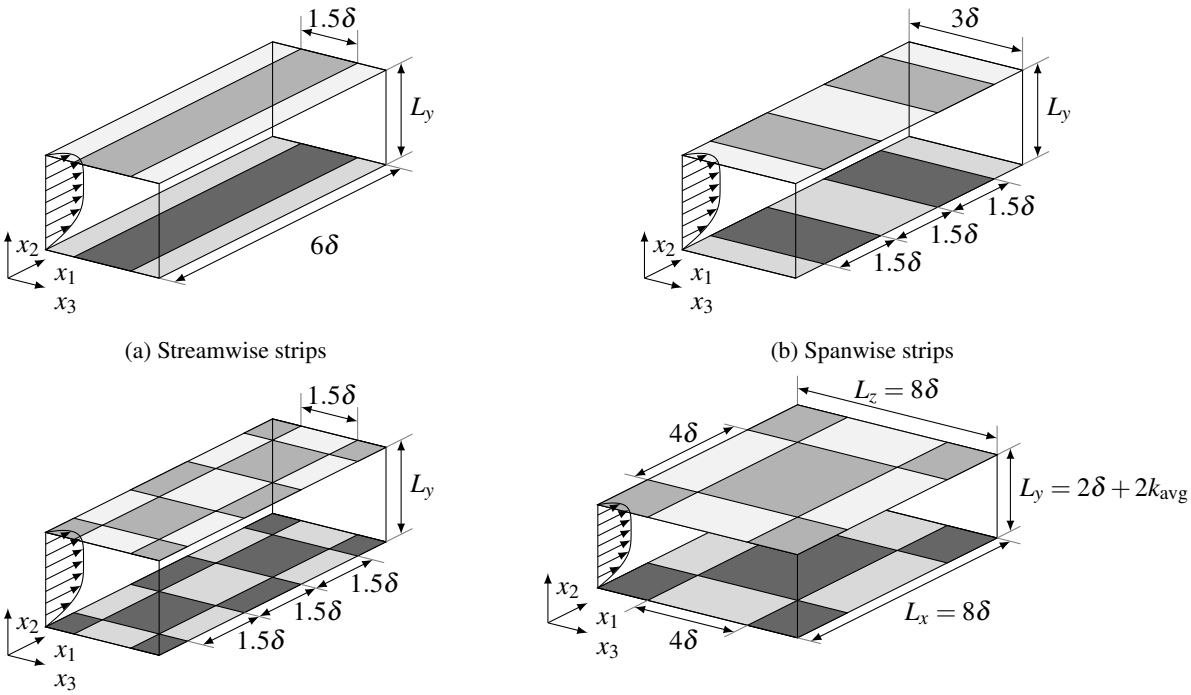

(a) Streamwise strips

(b) Spanwise strips

(c) Checkerboard pattern — small patch

(d) Checkerboard pattern — large patch

Figure 1: Simulation Setup for the four investigated channels, where black shading represents areas with roughness.

anemometry experiments with 4δ roughness strips at bulk Reynolds numbers ranging up to $Re_b = 50000$ conducted in a high precision channel flow facility as presented in Schmidt *et al.* (2026). These flow regimes are currently out of reach for direct numerical simulations. The streamwise velocity component is measured using a DANTEC StreamLine Pro 90N10 frame in conjunction with a 90C10 constant temperature anemometer. A straight single wire probe by DANTEC, equipped with a tungsten wire of about 1.25 mm length and 5 µm diameter, is used for the measurements.

RESULTS

Global Friction Factor

Since the flow is driven by a constant pressure gradient, the volume flow rate reduces due to the insertion of rough surface patches. The reduction of the corresponding dimensionless bulk velocity U_b results in an increase of the global friction factor, computed as

$$C_f = 2/U_b^2. \tag{5}$$

For the three different roughness arrangements, we obtain $C_f^{\text{span}} = 0.00993$, $C_f^{\text{stream}} = 0.00918$, and $C_f^{\text{patch}} = 0.00977$. Taking the checkerboard patch as reference, the streamwise strips result in 6% lower C_f, whereas the spanwise strips yield a friction factor that is 2% higher, despite identical roughness coverage ratio and the same Re_τ.

Flow Fields for Different Roughness Patch Arrangements

In the three different configurations, distinct flow features become apparent, as shown in three wall-parallel slices close to the wall (see fig. 2a, 2c and 2d). Placing a streamwise roughness strip of 1.5δ width into the channel leads to an increase in the streamwise velocity above the roughness compared to the smooth part, as visible in fig. 2b at a wall distance of $x_2/\delta \approx 0.6$. This behavior might arise due to the presence of turbulent secondary motions of Prandtl's second kind. Here, positive wall-normal velocities are developing over the smooth part, whereas above the roughness strip, negative wall-normal velocities are present, leading to a rotational motion. These rotational characteristics and their footprint on the streamwise flow field are well-known from literature (see e.g., Hinze (1973)). We note that this footprint is less pronounced in the DNS data than reported for the experiments by Frohnapfel *et al.* (2024), which might be a low Reynolds number effect. Close to the wall, the location of low- and high-speed fluid is reversed such that lower flow velocities are found over the rough surface (see fig. 2a).

This near-wall region of the perpendicular roughness pattern is shown in fig. 2c. The spanwise strips induce a repeated acceleration and deceleration of the near-wall fluid. The switch from higher speeds (in red) to lower speeds (in blue) is found at some distance downstream of the smooth-rough intersection. This shift is related to the formation of an internal boundary layer at the start of the rough surface section. This internal boundary layer, which grows in streamwise direction, and highlights the effects of the rough wall with larger drag and lower flow velocity. Interestingly, the maximum velocity in the wall-parallel plane at $x_2/\delta \approx 0.09$ (see fig. 2c) is observed shortly after the leading edge of the roughness strip. This results from continuity, as the mass flow above the smooth and rough strips needs to be equal, and the roughness acts as a resistance to the flow close to the wall; hence the fluid outside the internal boundary layer needs to accelerate. The footprint of the streamwise heterogeneity and the corresponding repeated acceleration and deceleration close to the wall is visible in the streamwise velocity throughout the channel, as shown in fig. 3 for different wall distances. Above

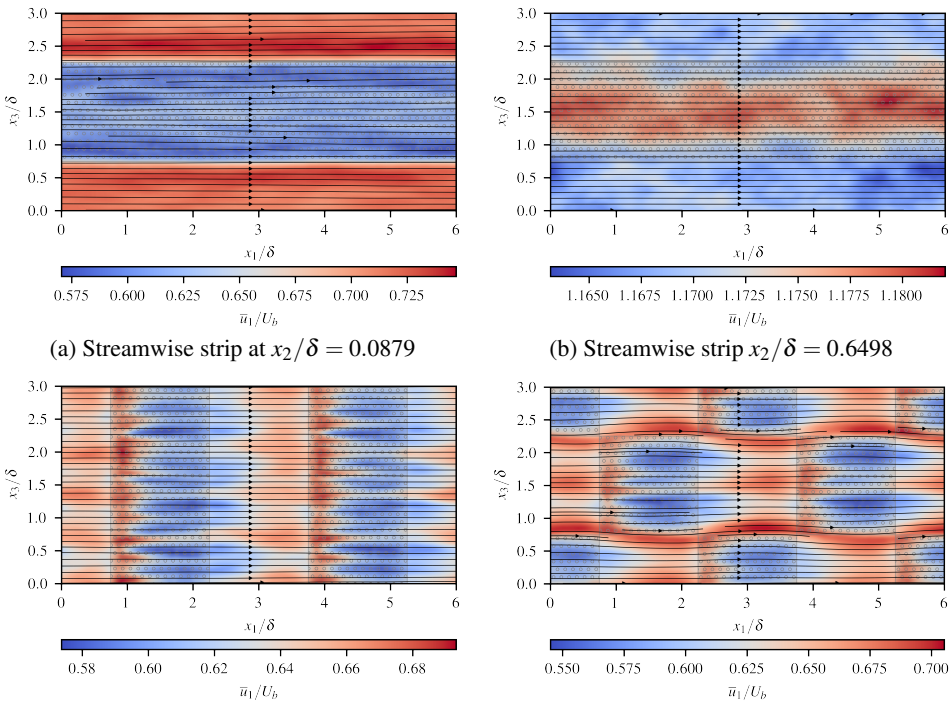

(a) Streamwise strip at $x_2/\delta = 0.0879$

(b) Streamwise strip $x_2/\delta = 0.6498$

(c) Spanwise strip $x_2/\delta = 0.0879$

(d) Checkerboard pattern $x_2/\delta = 0.0879$

Figure 2: Slices of the temporal averaged streamwise velocity normalized with bulk velocity at positions for the three investigated cases. The gray-colored area indicates the regions where the roughness is present.

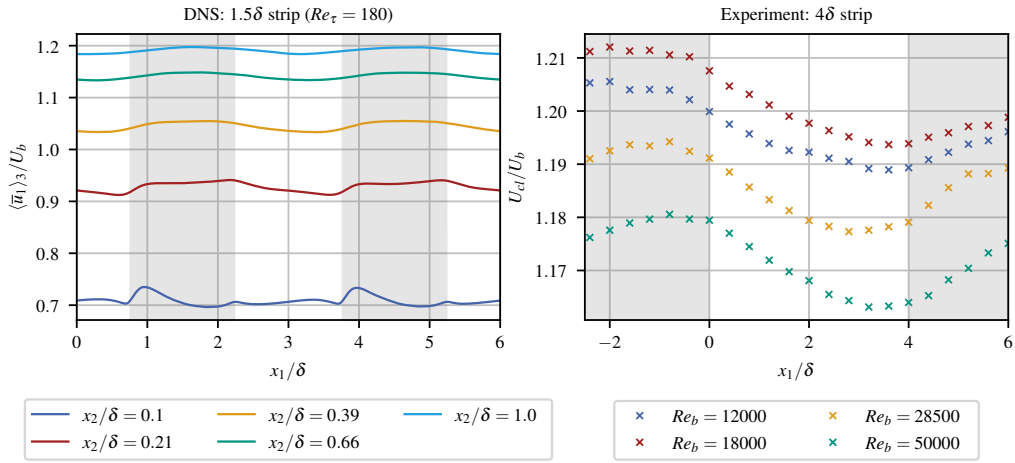

Figure 3: At different wall-normal positions, the streamwise velocity is accelerated and decelerated, aligning with the placement of spanwise strips. The temporally averaged streamwise velocity is spatially averaged in the homogeneous direction of the perpendicular strips (namely in x_3-direction) as indicated by $\langle \cdot \rangle_3$. The gray shaded areas correspond to the location of the roughness strips.

the roughness strip, the centerline velocity increases until its maximum in the second half of the spanwise strip. The continuous variation of the centerline velocity suggests that no fully developed flow state is reached. A similar behavior can be observed in experiments at higher Reynolds numbers and for larger patch sizes (see fig. 3 right). These results show a magnitude of U_{cl}/U_b which does not reveal a strong Reynolds number dependence. This magnitude is also in agreement with the simulation results, even though different strip widths are used.

Finally, in the near-wall region of roughness patches, as shown in fig. 2d, the repeated formation of an internal boundary layer is also clearly visible. In addition, we observe a distinct flow pattern in which regions with high streamwise velocities meander to avoid the rough surface. For the present patch roughness case, the flow pattern is only observed in the vicinity of the wall and does not extend to the channel centerline. Combining these observations with the skin friction factor suggests that the repeated formation of internal boundary layers is a key ingredient for the larger drag of the two cases with streamwise surface heterogeneity. This is reflected in the similarity of the respective global friction factors for spanwise strips and the checkerboard surface, which both show a formation of an internal boundary layer.

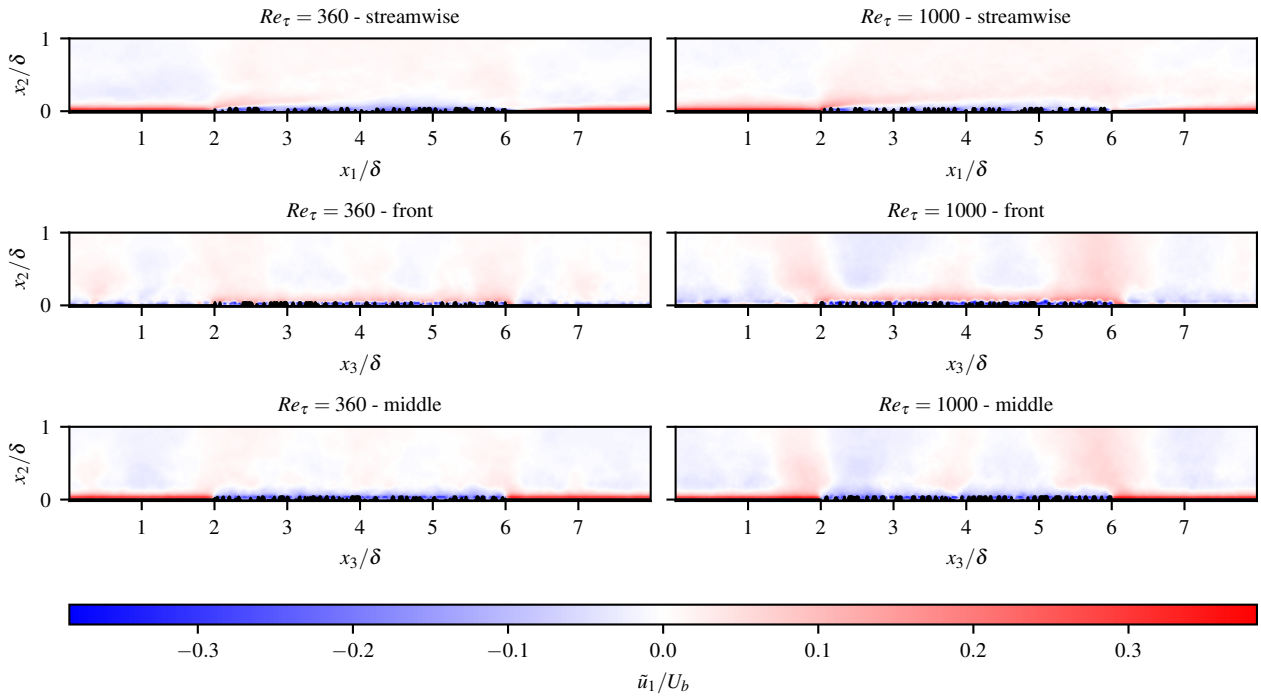

Figure 4: Influence of varying friction Reynolds number for the 4δ patch on the streamwise dispersive components. Upper column from a streamwise slice at $x_3/\delta = 4$ and lower two columns show spanwise profiles at $x_1/\delta = 2.18$ and $x_1/\delta = 4$.

Table 1: Overview on the different simulations and their corresponding bulk velocity.

Re_τ	s	s^+	U_b
180	1.5δ	270	14.30
360	4δ	1440	13.59
500	4δ	2000	13.23
1000	4δ	4000	13.29

Flow Fields over Checkerboard Roughness with Varying Patch Size

Besides the shape variations of different roughness heterogeneities, the influence of different checkerboard patch sizes is investigated. As indicated in fig. 1 the checkerboard case with $1.5\delta \times 1.5\delta$ patches is complemented by a case with patches of side length $s = 4\delta$. The investigated patch sizes in viscous units as well as their resulting bulk velocity are summarized in table 1. For the larger patch, the largest U_b is found for the lowest Re_τ which indicates that the friction coefficient of the patchy surface is lowest at $Re_\tau = 360$ and similar for the two higher Reynolds numbers, a tendency that is characteristic for rough surfaces.

To identify spatial flow field variations in the streamwise velocity component, we employ the concept of dispersive components using the triple decomposition (Reynolds & Hussain, 1972):

$$u_i(x_j,t) = \langle \overline{u}_i \rangle (x_3) + \tilde{u}_i(x_j) + u_i'(x_j,t), \tag{6}$$

splitting the velocity into an averaged component $\langle \overline{u}_i \rangle$, a position-dependent dispersive component $\tilde{u}_i$ and a fluctuating component u_i'. The first two combined form the local, temporally averaged mean velocity $\overline{u}_i(x_j)$. The dispersive component allows visualizing local deviations in the mean flow field. For wall-normal and spanwise velocity components it holds that $\langle \overline{u}_2 \rangle = \langle \overline{u}_3 \rangle = 0$. Therefore, for these two velocity components it holds that $\tilde{u}_i(x_j) = \overline{u}_i(x_j)$. In fig. 4 the dispersive part of the streamwise velocity component is displayed for $Re_\tau = 360$ and 1000. Shown in the upper row is a streamwise-wall-normal slice of the velocity field along the spanwise center of consecutive patches. The flow moves over a rough surface in the region $2 < x_1/\delta < 6$ and over smooth surface regions for smaller and larger values of x_1/δ. In contrast, in the second and last row of fig. 4 spanwise cuts at two different locations are displayed. Furthermore, the wall-normal and spanwise dispersive velocity components are shown in fig. 5, where wall-normal components are shown in the same cross-sectional plane as the dispersive streamwise velocity components. Spanwise components are displayed in spanwise slices close after the switch of smooth and rough patches.

Distinct characteristics can be identified, which are common to all investigated checkerboard cases and Reynolds numbers. Large dispersive components are confined to a region very close to the wall, whereas in regions further away from the wall the dispersive component diminish, indicating a homogeneous velocity distribution in streamwise direction. The spanwise slices, in contrast, show an alternating structure of positive and negative values of $\tilde{u}_1/U_b$. Positive values correlate with the spanwise edges of the roughness patch. Further positive-valued structures are present in the middle of the patches, where structures above the smooth patch are less dominant and decrease in clarity when moving in the streamwise direction. This spatial heterogeneity becomes more articulated for the larger patch size and for increasing friction Reynolds numbers and is limited to regions away from the wall. Directly over the rough surface section, negative $\tilde{u}_1$ and thus lower flow velocities are found, while positive values are

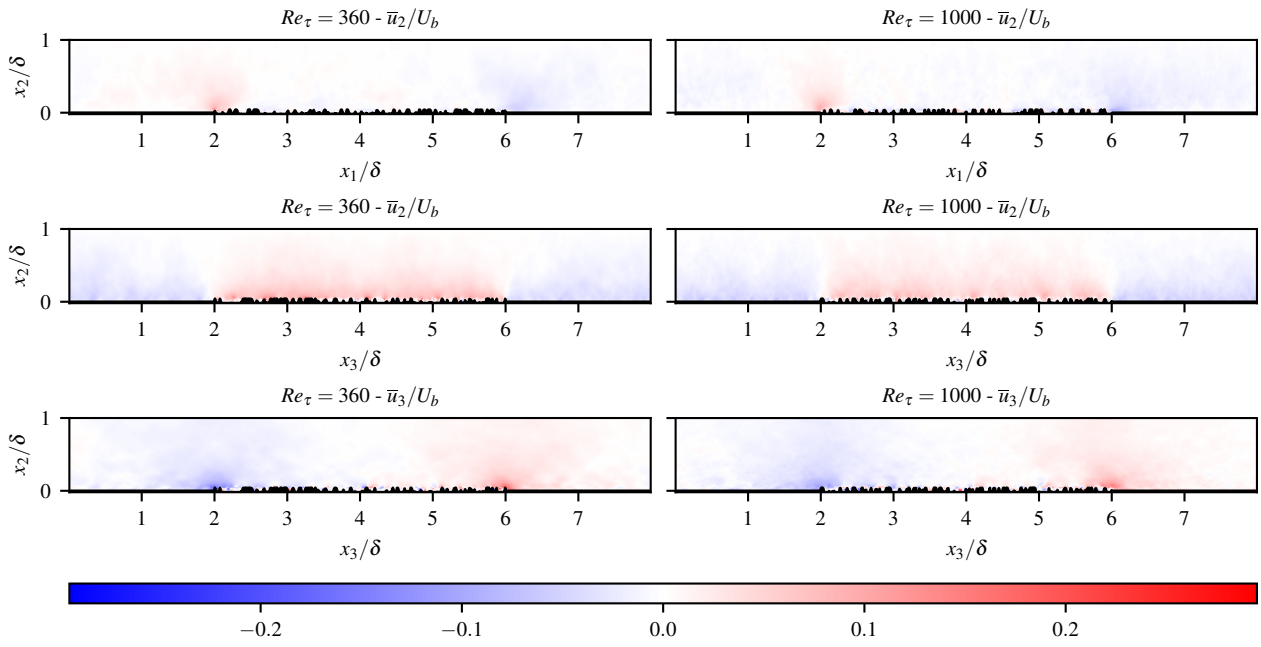

Figure 5: Influence of varying friction Reynolds number for the 4δ patch on the respective dispersive components. The wall normal component is shown in a streamwise slice at $x_3/\delta = 4$ (top row) as well as a spanwise slice at $x_1/\delta = 2.18$ (middle row), whereas the spanwise component is only shown in a spanwise slice at $x_1/\delta = 2.18$ (bottom row).

located over the smooth surface sections. In particular, the high-speed region over the smooth surface section is observed to be shifted upwards when the flow reaches the rough section. This can be identified in the spanwise slices as well, where the negative $\tilde{u}_1$-regions are smaller in wall-normal extent at the start of the patch compared to the center. Here a clear relation the formation of an internal boundary layer over the rough patch that induces a wall-normal displacement can be drawn – a feature also evident in the mean streamwise component (omitted for brevity). The corresponding upward displacement can be seen in fig. 5 in which $\overline{u}_2$ is shown in the same streamwise cross-sectional plane. It is interesting to note that positive wall-normal velocity values are present along the whole smooth-to-rough transition line (e.g., from $2 < z/\delta < 6$ in the middle row of fig. 5), and only minimal magnitude declines are visible towards the edges. A corresponding downward motion (negative $\overline{u}_2$) is located at the downstream end of the rough patch.

In respect to fig. 2d, it was already discussed that the near-wall flow is diverted sideways at the upstream edge of the 1.5δ roughness patch, unlike the strictly vertical displacement induced by the spanwise strips. This spanwise meandering motion is also found for the 4δ patch and visualized in fig. 5 in which the spanwise velocity component at $x_2/\delta = 2.18$ is shown. This location is shortly behind the smooth-to-rough transition. This meandering behavior can be seen in the negative and positive values of the dispersive component close to the left and right edges of the patch. These spots are not present in downstream spanwise slices at the middle of the patch (not shown for brevity), indicating a localized effect near the leading corners of the patch, where a clear pathway from smooth-to-smooth patch is visible. Interestingly, non-zero components of $\overline{u}_3$ are clearly present up to the channel centerline, while $\tilde{u}_2$ and $\tilde{u}_1$ remain more localized. Both the magnitude of $\overline{u}_2/U_b$ and $\overline{u}_3/U_b$ were found to remain in similar orders for all considered cases, but the wall-normal extent of the region in which it is found appears to shrink with increasing Reynolds number. In viscous scaled units, the spanwise velocity component slightly increases, whereas for the wall-normal component no trend can be seen from the selected cross-sectional planes. Furthermore, the U_b-normalized magnitude of the streamwise dispersive velocity component as well as the viscous scaled counterpart become larger for increasing friction Reynolds numbers, indicating a more heterogeneous flow field for higher Reynolds numbers.

Combining the information gained from the different dispersive components shows the routes for fluid evading the roughness patch. This includes an upward motion at the leading edge, similar to the perpendicular strips of 1.5δ width, and a localized spanwise motion forming meandering structures as already visualized for the smaller heterogeneity.

Reynolds stresses of 4δ Patches

As a final step, the Reynolds stress tensor can be evaluated, computed as $R_{pq} = \overline{u'_p u'_q} = \overline{(u_p - \overline{u}_p)(u_q - \overline{u}_q)}$, where the temporal mean is given by $\overline{u}_p = \langle \overline{u}_p \rangle + \tilde{u}_p$.

Again, the analysis is conducted by analyzing the two-dimensional slices in the streamwise direction for different Reynolds numbers and the larger $4\delta \times 4\delta$ patch (see fig. 6). Three observations can be made. First, the elevated values of $\overline{u'_1 u'_1}$ above the roughness patch compared to the smooth part. In its spatially averaged form $\langle \overline{u'_1 u'_1} \rangle$ the absolute value is still smaller than the corresponding smooth channel (not shown for brevity), which is in agreement with literature data reporting a dampening of the streamwise fluctuations for rough surfaces. A potential explanation can be rooted in the development of an internal boundary layer after the transition from smooth to rough and a not yet fully developed flow state.

Second, in the $\overline{u'_1 u'_1}$ component, a region of higher values evolves behind the rough-to-smooth transition. With reference to Schmidt *et al.* (2026), this region can be identified as a stress bore. As indicated by their hot-wire anemometry measure-

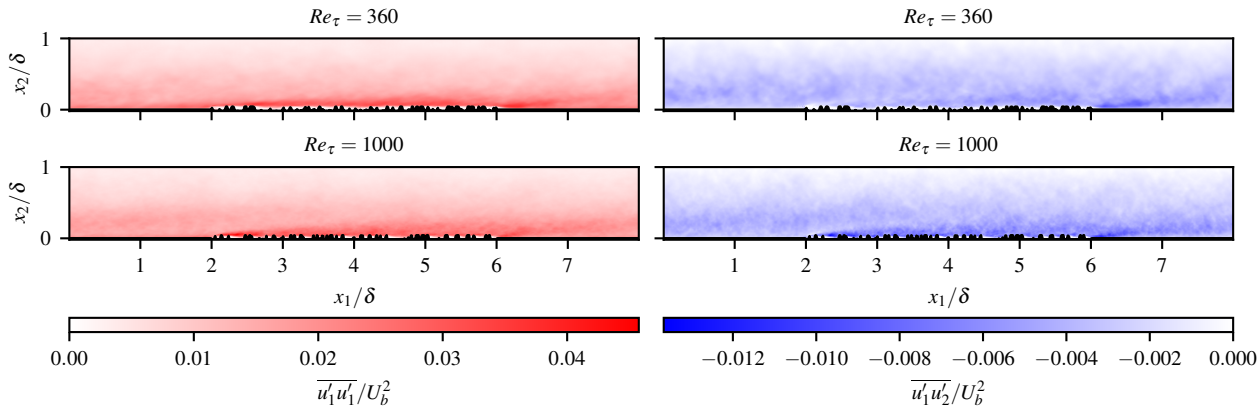

Figure 6: Influence of varying friction Reynolds number for the 4δ patch on the respective Reynolds stresses.

ments, the stress bore is lifting towards the channel center as a new internal boundary layer evolves after the rough-to-smooth transition. This behavior becomes less prominent for increasing friction Reynolds numbers, as seen in fig. 6. A similar region can be clearly identified in the $\overline{u_1'u_2'}$ component, with large negative values starting after the rough-to-smooth transition and moving away from the channel wall. Here, a second occurrence of this behavior is visible starting shortly after the smooth-to-rough transition, coinciding with the evolution of another internal boundary layer. It is furthermore interesting to mention, that especially the stress bore after the rough-to-smooth transition can be identified in the $\overline{u_2'u_2'}$ component as well. The observation of the stress bores in the different Reynolds stress tensor components in this numerical study further supports their importance for the flow heterogeneity, even though Schmidt *et al.* (2026) do not report the appearance of a clearly formed stress bore for their lowest Reynolds number of $Re_b = 12000$. An effect of different roughness realizations cannot be excluded, hence calling for a holistic investigation of different sandpaper recreations and their influence on the fluid flow. Finally, the magnitudes of the different Reynolds stress tensor components do not show a distinct Reynolds number dependency. Nevertheless, the regions with the distinct stress bores appear more articulated for higher Reynolds numbers.

CONCLUSION AND OUTLOOK

Canonical heterogeneous rough surfaces were shown to carry different distinct flow features, despite the fact that they are all composed of the same amount of rough and smooth surface area. Streamwise roughness strips with dimensions of 1.5δ at fixed $Re_\tau = 180$ show a clear presence of turbulent secondary motions. The repeated development of internal boundary layers in the flow above spanwise strips reflects in clear streamwise variations of the centerline velocity. Such continuous variations were also found in experimental data at larger Reynolds numbers and larger strip widths, indicating that the flow does not reach a fully developed state at any point. The two differently sized checkerboard surfaces, which carry both streamwise and spanwise inhomogeneity, indicate similar formation of internal boundary layers, whereas the development of clearly visible, strong turbulent secondary motions could not be observed in this configuration. The most distinct flow feature for this configuration is the presence of a near-wall high-speed pathway that develops in a wavy pattern along the edges of the smooth surface patches. These patterns are observed for viscous scaled patch sizes of $s^+ \in \{270; 1440; 2000; 4000\}$. The roughness-avoiding flow structures are apparent in the dispersive velocity components, for example, in the upward-downward motion in the streamwise slice over the patch midline or the left and right motion at the leading edge of a patch after a smooth-to-rough transition. Furthermore, the evolution of alternating stress bores can be observed in multiple Reynolds stress tensor components, indicating their important influence on flow heterogeneity. In future studies the influence of the roughness realization on the identified flow patterns should be further investigated to identify influences of both roughness length scales, namely of the roughness elements and the roughness patch size.

Acknowledgements: We greatly acknowledge the support by the German Research Foundation (DFG) under research project 561486292 and the computing time provided on the high-performance computer HoreKa by the National High-Performance Computing Center at KIT (NHR@KIT).

REFERENCES

Costa, P. 2018 A FFT-based finite-difference solver for massively-parallel direct numerical simulations of turbulent flows. *Computers & Mathematics with Applications* **76** (8), 1853–1862.

Frohnapfel, B., Deyn, L. von, Yang, J., Neuhauser, J., Stroh, A., Örlü, R. & Gatti, D. 2024 Flow resistance over heterogeneous roughness made of spanwise-alternating sandpaper strips. *Journal of Fluid Mechanics* **980**, A31.

Hinze, J. O. 1973 Experimental investigation on secondary currents in the turbulent flow through a straight conduit. *Applied Scientific Research* **28** (1), 453–465.

Jensen, R. M. & Forooghi, P. 2025 A study of turbulent flow over patchy roughness. *Journal of Fluid Mechanics* **1006**, A28.

Reynolds, W. C. & Hussain, A. K. M. F. 1972 The mechanics of an organized wave in turbulent shear flow. Part 3. Theoretical models and comparisons with experiments. *Journal of Fluid Mechanics* **54** (2), 263–288.

Schmidt, C., Sujar-Garrido, P., Schmitgen, U. & Frohnapfel, B. 2026 Influence of Reynolds number on the Pressure Gradient of Turbulent Channel Flow with Heterogeneous Roughness. *Journal of Fluid Mechanics* [Accepted for publication].

Shi, Z, Khorasani, S. M. H., Shin, H., Yang, J., Lee, S. & Bagheri, S. 2025 Drag prediction of rough-wall turbulent flow using data-driven regression. *Flow* **5**, E5.